Article

Ultralow Dark Current Density of Organic Photodetectors and Organic Light-Emitting Diodes Endowed by Highly Thermally Stable Derivatives of 2,7-Di-*tert*-butyl-9,9-dimethyl-9,10-dihydroacridine and Phenanthroimidazole Exhibiting Balanced Bipolar Charge Transport

Rita Butkute, Ausrine Masiulyte, Ehsan Ullah Rashid, Svetlana Sargsyan, Neelalohith Satish Moudgalya, Karolis Leitonas, Dmytro Volyniuk, and Juozas V. Grazulevicius*

Cite This: *ACS Appl. Electron. Mater.* 2024, 6, 4735–4745

Read Online

ACCESS | 📊 Metrics & More | 📖 Article Recommendations | 🔵 Supporting Information

ABSTRACT: Seeking to develop more advanced organic photodetectors (OPDs) and organic light-emitting diodes (OLEDs), we designed three derivatives of 2,7-di-*tert*-butyl-9,9-dimethyl-9,10-dihydroacridine and phenanthroimidazole with either $-CF_3$ or $-C(CH_3)_3$ groups. These compounds were synthesized by Buchwald−Hartwig amination reaction with yields of up to 77%. They show high glass transition temperatures above 200 °C and balanced electron and hole transport with mobilities of up to 10^{-3} $cm^2/V\cdot s$ under strong electric fields. One compound with $-C(CH_3)_3$ groups outperformed the standard host material in the OLED, which showed 17% higher external quantum efficiency. The low dark current density resulted in enhanced efficiency of OLEDs due to minimal charge leakage. Compared to the commercial material 1,1-bis[(di-4-tolylamino)phenyl]cyclohexane (TAPC), this compound allowed achieving superior photosensitivity in OPDs. The photocurrent to dark current density ratio at a reverse voltage of −10 V was found to be 6000. For TAPC-based OPDs, this ratio was only 43.3. The dark current density was significantly reduced to 4.5×10^{-7} mA·cm^{-2}, compared to 3×10^{-4} mA·cm^{-2} for TAPC-based OPDs at the same reverse voltage, thus enhancing the photosensitivity of the OPDs.

KEYWORDS: phenanthroimidazole, acridine, bipolar charge transport, organic semiconductor, organic light-emitting diode, organic photodetector
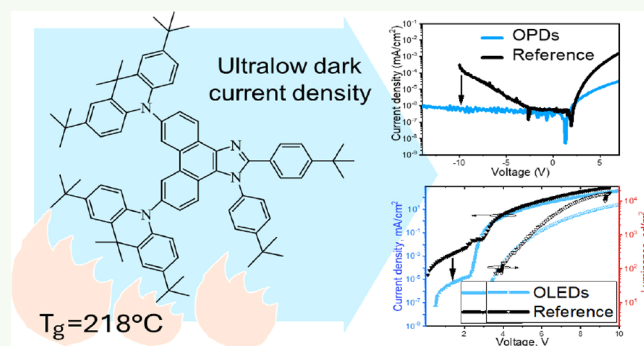
◼ INTRODUCTION

The further progress of society is, to a great extent, dependent on the development of technologies of flexible/wearable/transparent/stretchable electronics, as well as on the success in human health care/treatment/monitoring, biomedical imaging, development of electronic skins (e-skins), etc.[1−3] The conventional inorganic photodetectors and light-emitting diodes cannot fully meet the requirements of these technologies because of the mechanical rigidity, limited transparency, possible toxicity, cost inefficiency of the devices, and complexity of the fabrication technologies. In contrast, organic photodetectors (OPDs) and organic light-emitting diodes (OLEDs) meet the market demands due to their inherent flexibility, possible biocompatibility, simple fabrication by vacuum and wet methods, wide tunable physical properties, etc.[4−9] OLEDs and many OPDs are based on the structures of organic diodes, with layers of organic semiconductors (OSCs) as light-emitting layers or light-absorbing

layers, respectively.[10−12] OPDs can be characterized by internal gain mechanisms leading to the photomultiplication of carrier charges with the absorption of one photon.[13] In the case of diode-like OPDs, the gain can be obtained by the circulation of majority carriers in the light-absorbing layer of a single material or in donor−acceptor heterojunctions before the final recombination.[12] As a result, they can be characterized by an external quantum efficiency higher than 100%. For example, vacuum-deposited OPDs with a maximum external quantum efficiency (EQE) of 1 000 000% were developed exploiting the system consisting of 1,1-bis[(di-4-tolylamino)phenyl]-
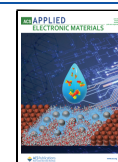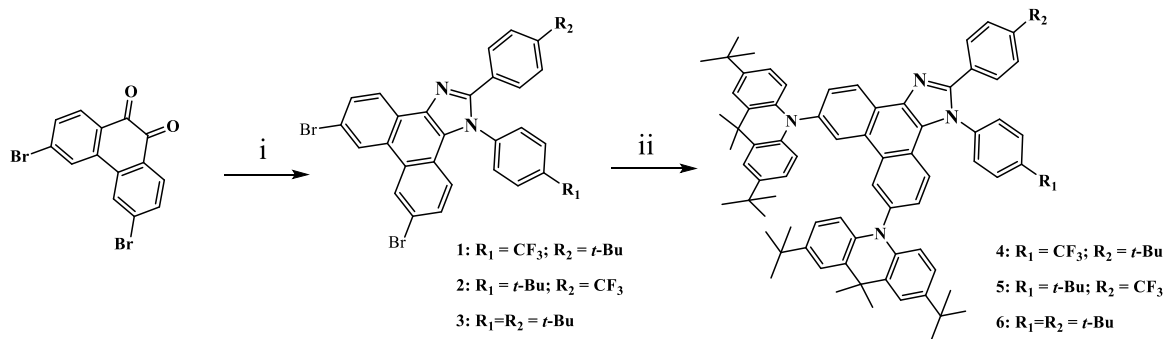
Scheme 1. Synthesis of Phenanthroimidazoles 1−6[a]

[a]Conditions: (i) 3,6-dibromophenanthrene-9,10-dione, 4-(*tert*-butyl)benzaldehyde (or 4-(trifluoromethyl)benzaldehyde), 4-(trifluoromethyl)-aniline (or 4-(*tert*-butyl)aniline), ammonium acetate, acetic acid, 1 h, 90 °C; (ii) 2,7-di-*tert*-butyl-9,9-dimethyl-9,10-dihydroacridine, *t*-BuONa, Pd(*t*-Bu₃)₂, toluene, 30 min, 110 °C.

cyclohexane (TAPC) and fullerene C6.[14] Despite the extremely high EQE values reached for OPDs, their specific detectivity remains low and is typically limited by the dark current density under reverse bias.[15,16] The dark current density of OLEDs is mostly left without attention despite the evidence that high dark current density affects the EQE of OLEDs.[17] In this study, we aimed to develop multifunctional OSCs applicable to the development of OPDs and OLEDs with reduced dark current density. The OSCs used were derivatives of 2,7-di-*tert*-butyl-9,9-dimethyl-9,10-dihydroacridine and phenanthroimidazole with either $-CF_3$ or $-C(CH_3)_3$ groups. We studied the effect of dark current densities on the performance of the OPDs and the OLEDs.

Phenanthroimidazole derivatives are studied as emitters and matrices for emissive layers of OLEDs because of their efficient blue emission,[18,19] bipolar charge transport properties,[20] and excellent thermal stability.[21] These properties make the phenanthroimidazole moiety an excellent "building block" for the development of materials not only for OLEDs but also for OPDs. The different nitrogen atoms (pyrrole-type (N1) and pyridine-type (N3)) of the phenanthroimidazole moiety determine the bipolar nature of this unit.[22] Phenanthroimidazole derivatives with substituents at N-1 and C-2 positions are more common[23] due to the simplicity of their chemical and structural modification. However, phenanthroimidazole derivatives with substituents at the C-6 and C-9 positions of phenanthroimidazole are considerably less studied.[24] Modification of structures via appending a trifluoromethyl group encourages weak H···F hydrogen-bonding interactions, which can promote backbone planarity.[25] Due to the electronegativity of the fluorine, electrons are pulled from the backbone to stabilize frontier molecular orbitals, thus influencing the electron transporting properties and intermolecular interactions.[26−28]

With the above-expressed aim, we report on the synthesis and investigations of three bipolar electroactive compounds having electron-accepting phenanthroimidazole moieties modified with $-CF_3$ and $-C(CH_3)_3$ groups and electron-donating 2,7-di-*tert*-butyl-9,9-dimethyl-9,10-dihydroacridine units. In order to reveal the multifunctionality of phenanthroimidazole derivatives, the applicability of the compounds in the OLEDs and the OPDs is demonstrated. The above-mentioned TAPC-based OPDs were selected as the reference devices. Using one of the developed compounds, the dark current density was significantly reduced to 4.5×10^{-7} mA·cm^{-2}, compared to $3 \times$

10^{-4} mA·cm^{-2} observed for TAPC-based OPDs at the same voltage. As a result, the photosensitivity of the peptides of the OPDs was significantly enhanced. The same compound allowed us to reach the lowest dark current density in the OLEDs, which showed an EQE 17% higher relative to that of the reference device in which the commercial host *N,N′*-di(1-naphthyl)-*N,N′*-diphenyl-(1,1′-biphenyl)-4,4′-diamine (NPB) was used.

EXPERIMENTAL SECTION

Procedures of the synthesis of the derivatives of 2,7-di-*tert*-butyl-9,9-dimethyl-9,10-dihydroacridine and phenanthroimidazole, identification, and characterization of common physical properties of the compounds are described in the Supporting Information, Experimental section.

OLEDs were fabricated by vacuum deposition of organic and metal layers onto precleaned indium tin oxide (ITO)-coated glass substrates under vacuum higher than 2×10^{-6} mbar. The rate of deposition was kept in the range of 0.7−1.0 kA/s for organic materials and of 0.8−1.2 kA/s for aluminum. All the materials that were used for the fabrication of the devices (except the synthesized ones in this work) were purchased from reputable commercial sources (Ossila, Merck) with the certificates of purity. ITO-coated glass substrates with a sheet resistance of 15 Ω/sq prepatterned for six pixels with an area of 4.5 mm^2 each were purchased from Ossila. The substrate surfaces were cleaned by sonication for 10 min in Hellmanex cleaning concentrate solution, followed by 10 min in distilled water, 10 min in isopropyl alcohol, and drying by a nitrogen gun. Afterward, the substrates were subjected to UV ozone treatment for 15 min. The light−current−voltage characteristics were recorded utilizing a certificated PH100-Si-HA-D0 photodiode together with the PC-based power and energy monitor 11S-LINK (from STANDA) and Keithley 2400C source meter. Electroluminescence (EL) spectra were taken by an Avantes AvaSpec-2048XL spectrometer. OLED efficiencies were calculated using the luminance, current density, and EL spectra.

OPDs were prepared by the procedure described above for the OLEDs. The current−voltage characteristics were recorded using a Keithley 2400C source meter, which was controlled during the experiment by the free software SweepMe! (sweep-me.net). Reverse biased voltage sweep parameters were 0.01 V/s taking 5 measurements every second (0.002 V increment steps). The current−voltage characteristics were collected in the dark, under indoor light, and under sunlight. The intensity of the ambient indoor light was 0.5 mW/cm^2. The "on/off" characteristics were recorded using a solar simulator from Sciencetech (Canada) combined with a 1.5G filter providing 100 mW/cm^2 stable irradiation and controlling the aperture opening manually. For testing the sensitivity at different wavelengths, a set of Thorlabs FGK01 colored glass filter kits was used.
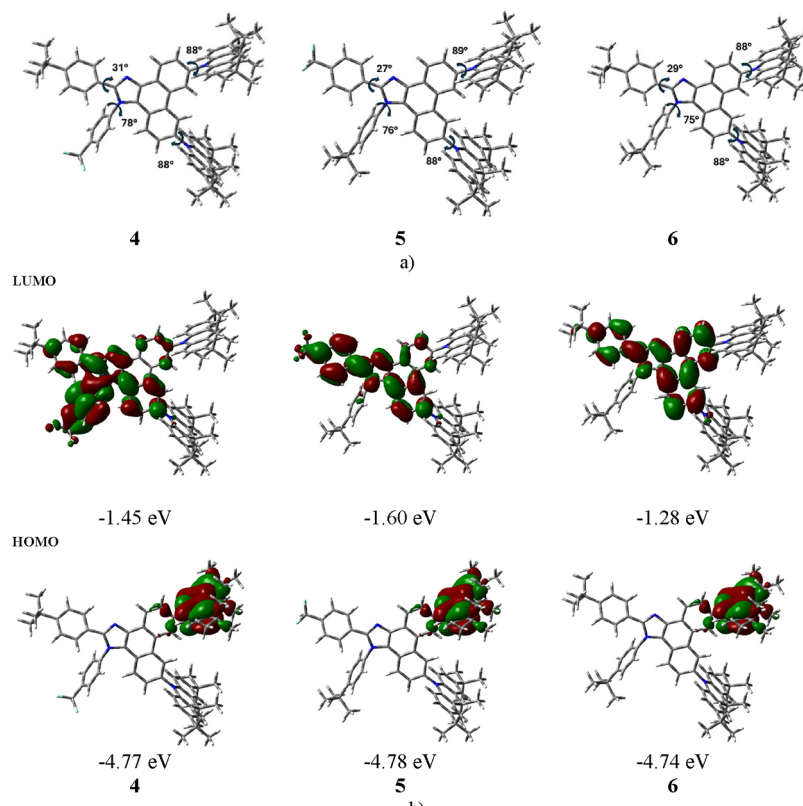
Figure 1. Optimized geometries (a) and HOMO and LUMO (b) of compounds 4−6 in toluene.
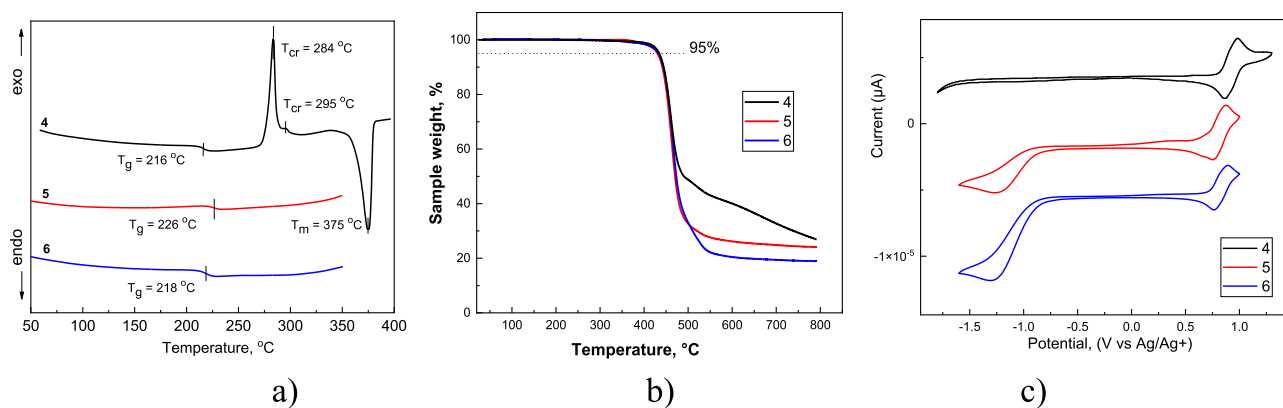

Figure 2. DSC second heating scans (a), TGA (b), and CV (c) curves of phenanthroimidazole derivatives 4−6.

■ RESULTS AND DISCUSSION

Synthesis and Identification. Phenanthroimidazoles 1−3 were obtained in high yields in a one-pot four-component condensation reaction of the corresponding aromatic aldehyde, amine, 3,6-dibromophenanthrenedione, and ammonium acetate using acetic acid as a solvent. The target compounds 4−6 were synthesized via a Buchwald−Hartwig amination reaction of intermediate phenanthroimidazoles 1−3 with 2,7-di-*tert*-butyl-9,9-dimethyl-9,10-dihydroacridine (Scheme 1). The structures of the compounds were confirmed by ^{1}H NMR, ^{13}C NMR, and IR spectroscopy, mass spectrometry, and elemental analysis (Figures S1−S9).

Geometries and Frontier Orbitals. All of the computations were performed at the theoretical level of B3LYP/6-31G(d,p). The theoretical optimized geometries of compounds 4−6 in toluene using the conductor-like polarizable continuum model (CPCM) are presented in Figure 1a. All attached substituents of phenanthroimidazole are twisted by dihedral angles of 27−89° with respect to the plane of the phenanthroimidazole core. The *tert*-butylated and methylated acridine moieties are almost right angled within the range of 88° to 89° with respect to the phenanthroimidazole core. Phenyl rings containing *tert*-butyl groups in the case of compounds 4 and 6 and those containing trifluoromethyl groups in the case of compound 5 are less twisted (range of 27−31°) when attached to the carbon atom of the phenanthroimidazole moiety. Meanwhile, the substituted phenyl rings when attached to the nitrogen of the phenanthroimidazole core are considerably more twisted (dihedral angles of 75−78°) owing to the existence of a lone pair of electrons on nitrogen repelling attached groups. This leads to high dihedral angles.

Table 1. Thermal, Photophysical, and Electrochemical Characteristics of Compounds 4−6

compound	$T_g{}^a$, °C	$T_{cr}{}^b/T_m{}^b$, °C	$T_d{}^c$, °C	$E_{ox}{}^d$ V	$IP_{CV}{}^d$ eV	$E_g^{opt,e}$ eV	$EA_{CV}{}^f$ eV	Φ_f (soln/film)^g	$S_1{}^h$ eV	$T_1{}^h$ eV
4	216	−/373, 389	427	0.807	5.18	2.99	2.19	0.03/0.05	3.19	2.86
5	226	−/392	421	0.713	5.08	3.15	1.93	0.07/0.09	3.17	2.68
6	218	−/367	422	0.738	5.11	3.24	1.87	0.03/0.07	3.17	2.70

[a]Glass transition temperatures obtained from second heating in DSC. [b]Melting and crystallization temperatures obtained from first heating in DSC. [c]Destruction temperatures obtained from TGA. [d]Onset oxidation potential vs Ag/Ag⁺. $IP_{CV} = (E_{ox} − E_{Fc/Fc+}) + 4.8$ (eV). [e]Estimated from the onset wavelength of optical absorption according to the empirical formula: $E_g^{opt} = 1240/\lambda_{edge}$, in which λ_{edge} is the onset value of the absorption spectrum in the long wave direction. [f]$EA_{CV} = IP_{CV} − E_g^{opt}$. [g]Fluorescence quantum yield of the solutions and solid state quantum yields estimated using an integrating sphere. [h]Singlet energy calculated from the graphs of photoluminescence at 77 K and triplet energy calculated from the graphs of phosphorescence at 77 K.
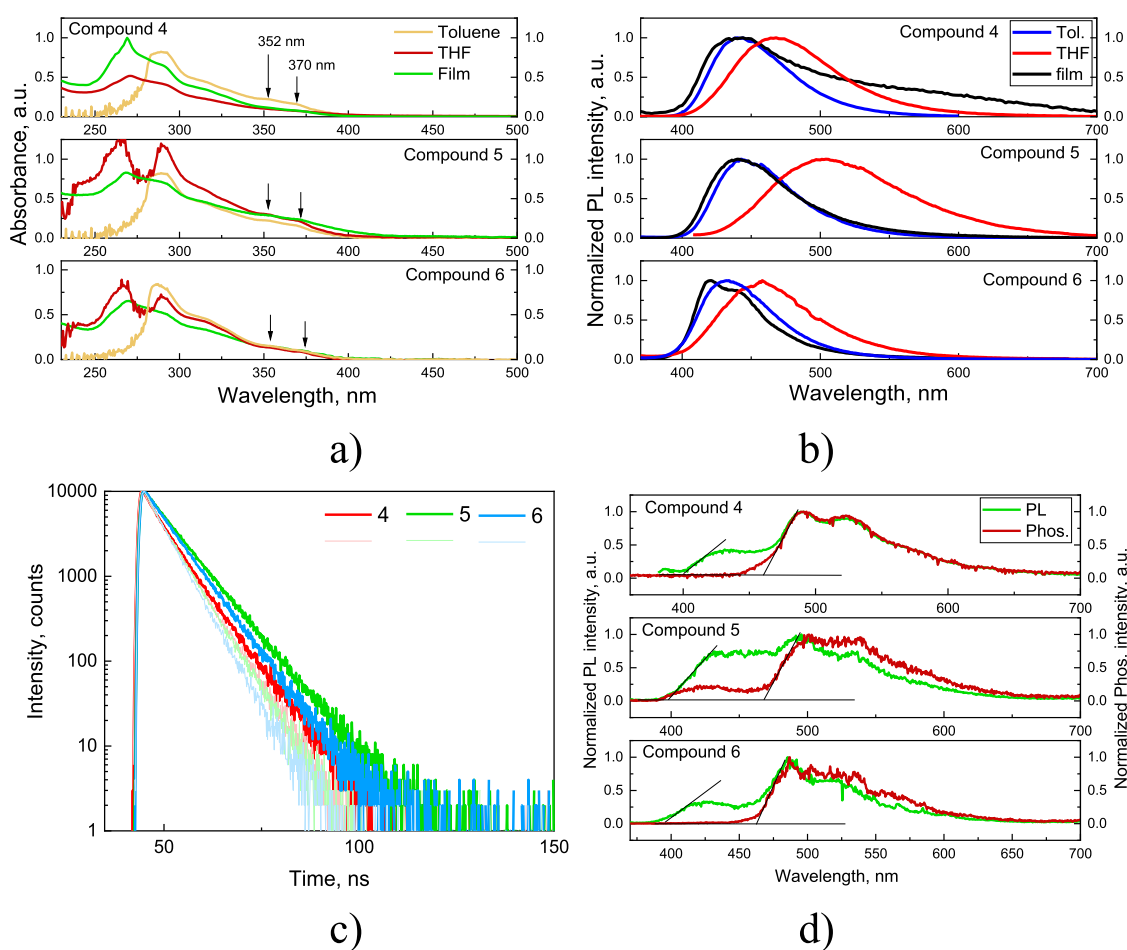

Figure 3. Absorption (a) and PL (b) spectra of toluene and THF solutions and the films of 4−6, PL decay curves (c) of air-equilibrated (thin lines) and deoxygenated (thick lines) toluene solutions of 4−6, and PL and phosphorescence (Phos.) spectra (d) of 2-Me-THF solutions of 4−6 recorded at 77 K. The concentration of the solutions of 4−6 was 1×10^{-5} M. Phos. spectra were recorded with a delay of 5 ms after excitation.

The calculated energy values of HOMO and LUMO, as well as topologies of molecular orbitals of compounds 4−6, are shown in Figure 1b. The wave function predominates in the HOMO of the three compounds on the electron-donating acridine with *tert*-butyl groups, with a small overlap on the phenanthroimidazole core. In the case of the LUMO of compounds 4 and 5, a slight existence of the wave function is on the phenanthroimidazole core and *tert*-butylated phenyl and more dominantly on phenyl rings containing electron-withdrawing trifluoromethyl groups. In the LUMO of compound 6, the wave function can be seen on the phenanthroimidazole core. The slight existence of a wave function on the *tert*-butylated phenyl attached to the nitrogen atom of phenanthroimidazole core is due to its high dihedral angle.

The intensive existence of a wave function on the other *tert*-butylated phenyl group attached to the carbon atom of the phenanthroimidazole core is due to its small dihedral angle. The analysis of energies of the frontier orbitals confirms the above statement. Higher HOMO and LUMO energies observed for compound 6 are apparently due to efficient conjugation between the core and phenyl substituents (Figure 1b).

Thermal, Electrochemical, and Photophysical Properties. The thermal properties of the phenanthroimidazole derivatives (4−6) were investigated by thermogravimetric (TG) analysis and differential scanning calorimetry (DSC) under a nitrogen atmosphere. The DSC and TG curves are presented in Figure 2a,b and Figure S10. The temperatures of

the transitions are summarized in Table 1. The compounds exhibited high thermal stability and a glass-forming ability. Their 5% weight-loss temperatures (T_d) exceeded 421 °C. During the TGA measurements, incomplete weight loss of the studied phenanthroimidazole derivatives was detected (Figure 2b), indicating thermal degradation but not sublimation of the samples. The compounds were obtained as crystalline substances after the synthesis and purification, and endothermic melting signals were observed in the first heating scans of the DSC measurements (Table 1, Figure S10). The second DSC heating scans of the compounds revealed glass transitions in the range from 216 to 226 °C (Figure 2a). The further heating of the sample of compound **4** above the glass transition temperature (T_g) revealed endothermic crystallization effects at 284 and 295 °C and the melting signal at 375 °C. The trifluoromethyl phenyl group at the N-1 position apparently enhances the inclination to crystallization of compound **4** due to the ability of the trifluoromethyl group to form intramolecular hydrogen bonds.[29] Very high T_g and T_d values of compounds **4−6** indicate that the amorphous layers of these compounds can be fabricated by the vacuum thermal evaporation technique. In addition, the solid amorphous layers of compounds **5** and **6** are expected to exhibit high morphological stability, which is desirable for the materials used in optoelectronic devices.

Electrochemical properties of synthesized compounds were studied by cyclic voltammetry (CV). The obtained electrochemical characteristics are given in Table 1. The CV curves of the solutions of the compounds in DCM are shown in Figure 2c. During the positive potential sweep, the compounds showed reversible oxidation peaks. The values of oxidation onset potentials against ferrocene (E_{ox} onset vs Fc/Fc$^+$) for compounds **4**, **5**, and **6** were found to be 0.807, 0.713, and 0.738 V, respectively. The compounds form stable radical cations; the same values of electrochemical peaks were observed for derivatives **4−6** after repeated cycles. The reason for the enhanced electrochemical stability of the compounds might be blocking of the active C-2 and C-7 positions of acridan moieties by *tert*-butyl groups. The ionization potentials derived from the CV measurements (IP$_{CV}$) for compounds **4−6** were found to be comparable, i.e., 5.18, 5.08, and 5.11 eV, respectively. IP$_{CV}$ values are similar and decrease in the order 4 > 6 > 5. The electron affinities (EA$_{CV}$) were estimated using optical bandgaps (E_g^{opt}). For compounds **4−6** they were estimated to be 2.19 1.93, and 1.87 eV, respectively.

The dilute solutions and films of compounds **4−6** were found to be transparent in the visible spectral region, as confirmed by the corresponding absorption spectra (Figure 3a). Time-dependent DFT (TD-DFT) estimations were done at the same level of theory (B3LYP/6-31G(d,p)), and the CPCM solvent model was used to study toluene solvent impact. The natural transition orbitals (NTOs) were generated to understand the nature of the transitions. The experimental absorption spectra of **4−6** align with the theoretical spectra (Figure S11). The intensive and broad experimental absorption peak (ca. 280−300 nm) of the toluene solution is shown as a combination of the different local excitation (LE) and charge transfer (CT) excited states by the TD-DFT study (Table S1). In the case of compound **4**, this intensive peak corresponds to S$_{18}$, S$_{19}$, and S$_{21}$ excitations. S$_{18}$ of compound **4** mainly possesses LE of alkylated acridine with very small CT to biphenyl phenanthroimidazole. S$_{19}$ shows LE of biphenyl phenanthroimidazole, while S$_{21}$ has LE at phenanthroimidazole

with small CT from alkylated acridine to biphenyl phenanthroimidazole (Figure S12). For compound **5**, S$_{18}$, S$_{20}$, and S$_{22}$ are the excitations corresponding to intensive absorption at ca. 290−300 nm. S$_{18}$ and S$_{20}$ show local excitation of alkylated acridine and CT to biphenyl phenanthroimidazole, while S$_{22}$ shows LE of biphenyl phenanthroimidazole and very small CT from alkylated acridine to phenanthroimidazole. In the case of compound **6**, S$_{14}$, S$_{17}$, S$_{20,}$ S$_{24}$, and S$_{25}$ are the most intensive excitations, of which S$_{14}$ shows combined LE and CT of alkylated acridine and biphenyl phenanthroimidazole. S$_{17}$ and S$_{24}$ give LE at alkylated acridine and minute CT to biphenyl phenanthroimidazole. S$_{20}$ gives a simple LE of biphenyl phenanthroimidazole. Meanwhile S$_{25}$ illustrates a simple LE of biphenyl phenanthroimidazole and small CT from alkylated acridine to phenanthroimidazole.

In the empirical spectra of all three compounds, very broad shoulder peaks can be observed at ca. 320 and 335 nm. As per TD-DFT results, S$_9$, S$_{11}$, and S$_{13}$ for compound **4**, S$_7$ and S$_9$ for compound **5**, and S$_6$ and S$_8$ for compound **6** are responsible for the LE excitations from the biphenyl phenanthroimidazole core corresponding to the broad shoulder peaks observed at ca. 320 and 335 nm.

TD-DFT results indicate that S$_1$−S$_8$, S$_1$−S$_6$, and S$_1$−S$_5$ transitions of compound **4**, **5**, and **6**, respectively, are complete CT from an alkylated acridine donor to a biphenyl phenanthroimidazole acceptor with small oscillator strength owing to the orthogonal plane between acceptor and donor of the molecules. These TD-DFT transitions match CT wide tail peaks of the experimental absorption spectra, which span from 350 to about 400 nm (Figure 3a). The empirical spectra of absorption show that the CT bands have higher absorption intensities than the predicted ones. This observation can be attributed to the empirically smaller dihedral angle between the donor and acceptor moieties compared to the theoretically calculated angles.

CT is clearly detected by analysis of the emissions of the solutions of **4−6** in the solvents of different polarity (Figure 3b). Toluene solutions of **4−6** emit deep blue light with nonstructured PL spectra peaking in the region of 430−444 nm. The PL spectra of THF solutions showed redshifts with respect to the spectra of the solutions in toluene. Because of the increased electron-accepting strength of electron-withdrawing fragments of compounds **4** and **5** caused by the presence of trifluoro methyl groups, PL spectra of their THF solutions showed stronger redshifts than that of a THF solution of compound **6** containing *tert*-butyl groups.

The dilute solutions of **4−6** in toluene were sensitive to the presence of oxygen (Figure S13). After deoxygenation, by purging with inert gas through the solutions for 3 min, the emission intensity of the toluene solutions increased by a factor of ca. 1.3. This observation demonstrates that triplet excited states of **4−6** are involved in the relaxation processes. Emission intensity increased because of either the reduced efficiency of intersystem crossing (ISC) or the induced efficiency of reverse intersystem crossing (RISC) when triplet relaxation is absent via triplet oxygen levels. The PL decay curves of the toluene solutions recorded before and after the deoxygenation differ (Figure 3c). Fluorescence lifetimes of about 5 ns were obtained for the deoxygenated toluene solutions of **4−6**. In addition, singlet−triplet energy splitting was greater than 0.33 eV for **4−6**, fully excluding thermally activated delay fluorescence (Figure 3d, Table 1). Films of **4−6** were characterized by similar PL spectra to those of toluene solutions. The
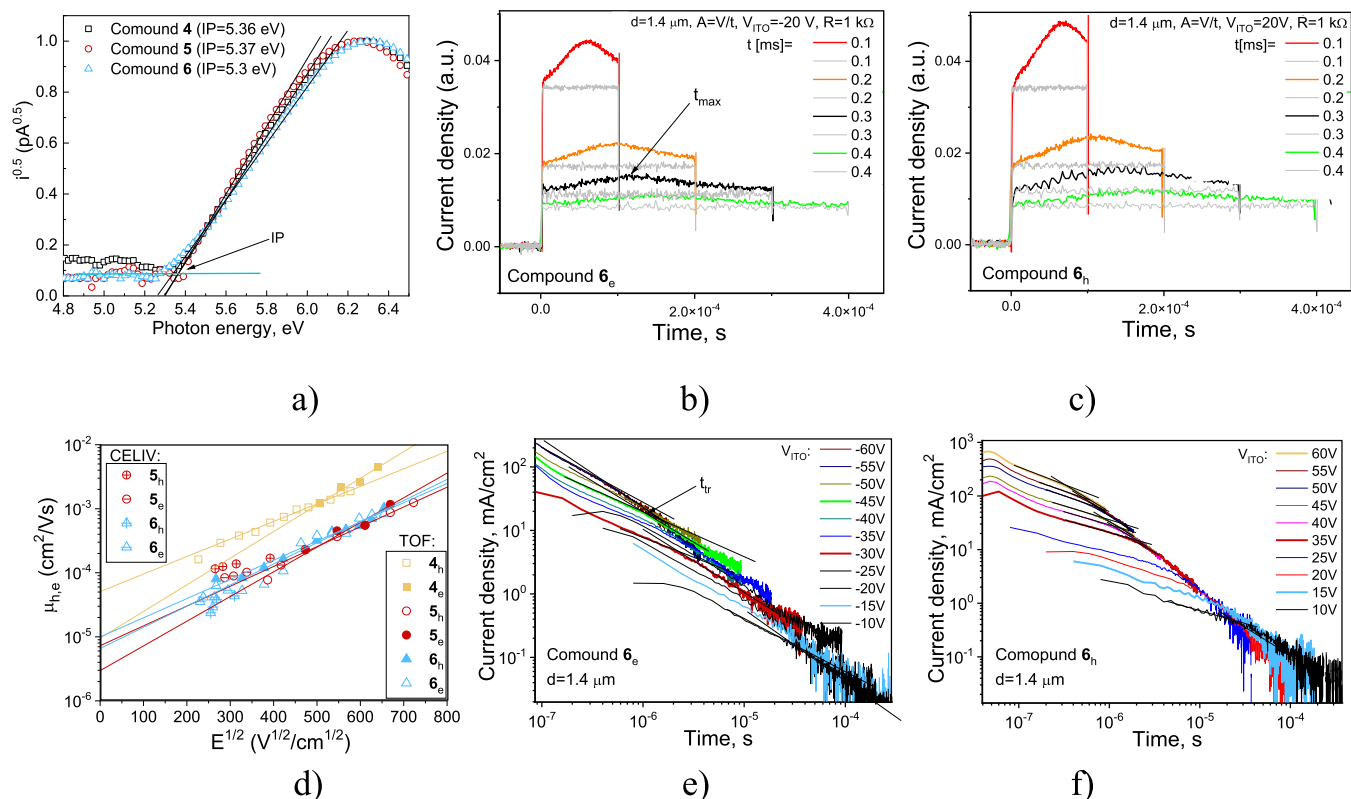
Figure 4. UPS spectra (a), CELIV signals (b, c) of the layer of compound **6**, and hole (μ_h) and electron (μ_e) mobility values (d) recorded at different electric fields (E) of vacuum-deposited films of phenanthroimidazoles **4–6** measured by TOF and CELIV methods. The gray curves in (b) and (c) are CELIV signals recorded without laser excitation. The lines in (d) correspond to the fitting. TOF signals correspond to electrons (e) and holes (f) observed for the film of compound **6**.

Table 2. UPS Data and Charge Mobility Parameters of the Films of 4–6

				electrons			holes		
compound	IP_{film}, eV	$E_g^{opt.}$, eV	EA_{film}, eV	μ_{0e}, cm^2 V^{-1} s^{-1}	β_e, (cm V^{-1})$^{1/2}$	$\mu_e{}^a$ cm^2 V^{-1} s^{-1}	μ_{0h}, cm^2 V^{-1} s^{-1}	β_h, (cm V^{-1})$^{1/2}$	$\mu_h{}^a$ cm^2 V^{-1} s^{-1}
4	5.36	2.99	2.37	9.6×10^{-6}	9.6×10^{-3}	3×10^{-3}	6.3×10^{-5}	6.3×10^{-3}	2.2×10^{-3}
5	5.37	2.98	2.39	3×10^{-6}	8.9×10^{-3}	6×10^{-4}	7.1×10^{-6}	7.1×10^{-3}	4.2×10^{-4}
6	5.30	3.11	2.19	1×10^{-5}	6.9×10^{-3}	6.2×10^{-4}	7.6×10^{-6}	7.6×10^{-3}	6.2×10^{-4}

^{a}Hole and electron drift mobilities at the electric field of 3.6×10^5 V·cm^{-1}.

fluorescence quantum yields of films of **4–6** were slightly higher, reaching 9%, compared to dilute toluene solutions (Table 1). Such values rather excluded applications of **4–6** as emitters. Despite the emission challenges, the triplet levels of **4–6** indicate that they can be utilized as hosts for light-emitting applications.

Photoelectrical Properties. The ionization potentials (IP_{film}) of the solid films of **4–6** were estimated by ultraviolet photoelectron spectroscopy (UPS) in air. The UPS spectra, photoelectron yields versus incident photon energy, are plotted in Figure 4a. For the thin vacuum-deposited films of **4–6** the IP_{film} values of 5.36, 5.37, and 5.3 eV, respectively, were estimated from the thresholds of UPS spectra. Practically the same thresholds were observed for the layers of **4–6**. This observation shows that the nature of substituents of phenyl groups has a negligible effect on IP_{film} values of the derivatives of 2,7-di-*tert*-butyl-9,9-dimethyl-9,10-dihydroacridine and di-phenyl phenanthroimidazole. For the solid samples of **4–6** the tentative electron affinities of 2.37, 2.39, and 2.19 eV were calculated by the formula $EA_{film} = IP_{film} - E_g^{opt}$. The optical bandgaps ($E_g^{opt}$) of 2.99, 2.98, and 3.11 eV taken from the

corresponding absorption spectra of the thin films were used for the calculations. The layers of **4–6** in the same device structure are expected to have similar hole and electron injection abilities. Nevertheless, compound **6**, containing *tert*-butyl substituents attached to phenyl groups, showed slightly different IP_{film} and EA_{film}, suggesting slightly different electronic properties of **6** in comparison to those of **4** and **5**, which contain trifluoromethyl substituents (Table 2).

Thick vacuum-deposited films of **4–6** in a two-electrode-based structure ITO/film/Al were probed using photoinduced charge carrier extraction by linearly increasing voltage (photo-CELIV) and time-of-flight (TOF) methods.[30] Dark-CELIV and photo-CELIV signals were recorded without and with laser excitation of the films through the optically transparent electrode ITO. The photo-CELIV signals with well-visible maxima at time t_{max} were recorded for compounds **4** and **5** (Figure 4b,c, Figure S14a). The maxima were not observed in the dark-CELIV signals (gray curves) recorded without laser excitation. The thicknesses (d) of the films of **4–6** were 3.9, 0.67, and 1.4 μm, respectively. Those thick films enable the surface generation of charges and the subsequent transport of
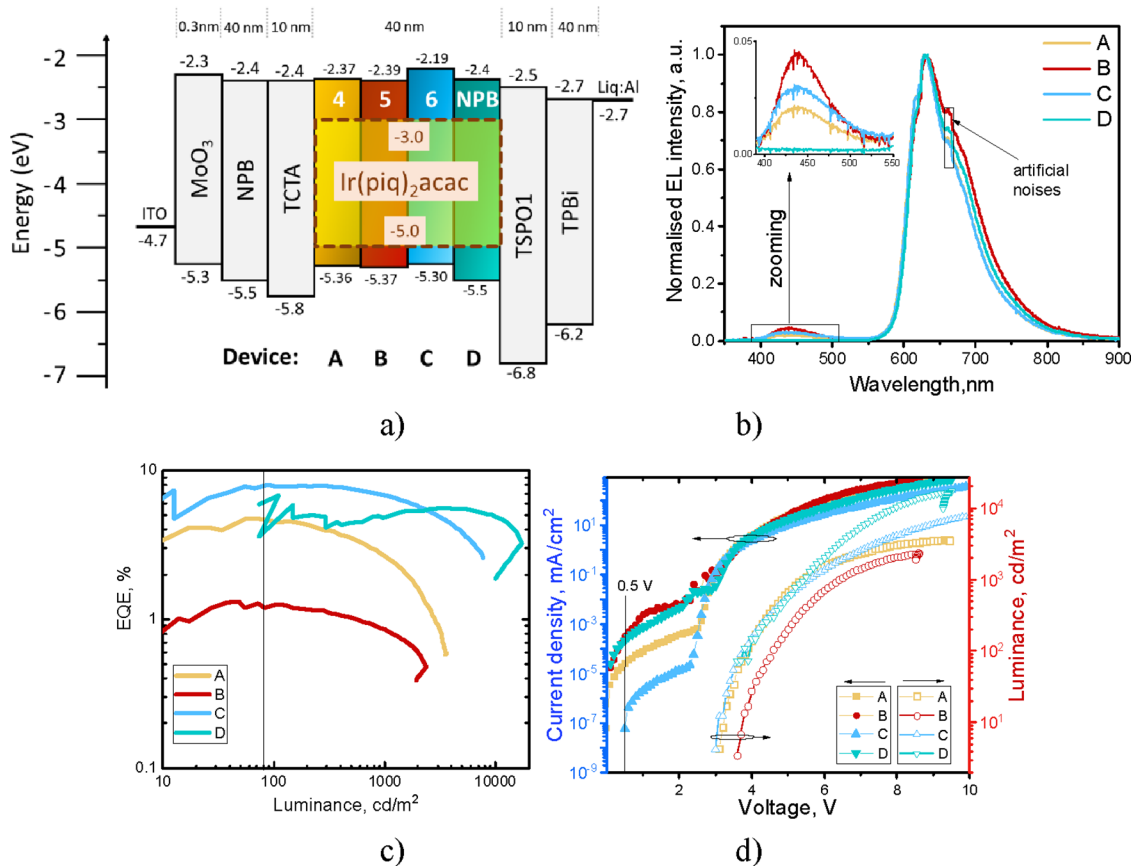
Figure 5. Equilibrium energy diagram (a), EL spectra (b), EQE dependence on luminance (c), and current density and luminance as a function of external voltages (d) of devices A−D.

electrons or holes through the layers. As a result, the different photo-CELIV signals described the transport of electrons or holes when negative or positive voltages (V) were applied to ITO, respectively. The photo-CELIV signals were collected at the voltage rise rate $A = V/t_{pulse}$. The different pulse durations (t_{pulse}) allowed us to obtain t_{max} values at the different electric fields (Figure 4b,c, Figure S14b). As a result, hole or electron mobilities ($\mu_{h,e}$) could be calculated at different electric fields. The formula $\mu_{h,e}^{CELIV} = 2 \cdot d^2/(A \cdot t_{max}^2)$ describing the case of the low conductivity and surface photogeneration was used.[31] The $\mu_{h,e}$ values estimated for the films of **5** and **6** are collected in Figure 4d. Because of the high thickness of the film of **4**, the electric fields at the applied maximum amplitude voltage of 20 V were too low for observation of photo-CELIV signals (Figure S14a). Fortunately, the high thicknesses of the films are appropriate for TOF measurements (Figure 4e,f, Figure S14b). Current transients with visible transit times (t_{tr}) for electrons and holes were recorded for **4−6** by applying negative or positive voltages to ITO, respectively, similarly to the above-described procedure of photo-CELIV. The $\mu_{h,e}$ values for **4−6** were calculated using the formula $\mu_{h,e}^{TOF} = d^2/(V \cdot t_{tr})$. The corresponding plots are shown in Figure 4d. The charge mobilities as a function of electric fields were plotted according to the function of Poole−Frenkel, $\mu_{h,e} = \mu_{0h,e} \exp(\beta_{h,e} \cdot E^{1/2})$. This function was utilized to fit the experimental data and determine the zero-field mobilities ($\mu_{0h,e}$) and field-dependent parameters ($\beta_{h,e}$) (Table 2).

The samples of compounds **4−6** were characterized by bipolar charge transport with similar mobility values in the wide range of electric fields (Figure 4d). A slight variation in

the charge mobility values of **4−6** at the different electric fields was observed due to the different values of $\beta_{h,e}$. For example, a μ_{0e} of 9.6×10^{-6} cm^2 V^{-1} s^{-1} and a μ_{0h} of 6.3×10^{-5} cm^2 V^{-1} s^{-1} were obtained for the film of **4** at a zero electric field. Because of the high β_e of 9.6×10^{-3} (cm V^{-1})$^{1/2}$ and β_h of 6.4×10^{-3} (cm V^{-1})$^{1/2}$, the high and balanced mobility values μ_e of 3×10^{-3} cm^2 V^{-1} s^{-1} and μ_h of 2.2×10^{-3} cm^2 V^{-1} s^{-1} were obtained for this film at the electric field of 3.6×10^5 V·s^{-1}. Despite relatively low and unbalanced mobility values of holes and electrons at zero electric fields, compounds **4−6** can show efficient and balanced charge transport at high electric fields. Such charge mobility parameters established for the films of **4−6** can be promising for their application in OLEDs working at high electric fields and requiring the balanced transport of holes and electrons, as well as for OPDs working at low electric fields and requiring unbalanced transport of holes and electrons.[12,8]

Performance in Organic Light-Emitting Diodes. Electronic properties of **4−6** were investigated in a red phosphorescent OLED. They were compared with those of the conventional hosting material NPB as the reference by using the same device structure. The idea to use compounds **4**, **5**, and **6** as hosts for the phosphorescent emitter bis(1-phenylisoquinoline)(acetylacetonate)iridium(III) (Ir(piq)$_2$acac) was based mainly on the favorable energy levels of the hosts and emitter (Figure 5a). The hosting materials are characterized by considerably higher triplet energies than those of Ir(piq)$_2$acac. Thus, loss of energy via the triplet channels was completely prevented. We selected only one concentration of 10 wt % of Ir(piq)$_2$acac in the hosts without the precise

optimization of devices based on the previous publication on red phosphorescent emitters.[31] This approach allowed us to compare the hosting properties of **4−6** and NPB without pursuit of the record performance of Ir(piq)$_2$acac-based OLEDs. The device structure ITO[100 nm]/MoO$_3$[0.3 nm]/NPB[40 nm]/TCTA[10 nm]/**host** [90 wt %]:Ir-(piq)$_2$acac[10 wt %][40 nm]/TSPO1[10 nm]/TPBi[40 nm]/LiF:Al[100 nm] was selected. We labeled devices A−D containing host **4**, **5**, **6**, or NPB, respectively (Figure 5a). Molybdenum trioxide (MoO$_3$), NPB, tris(4-carbazoyl-9-ylphenyl)amine (TCTA), diphenyl[4-(triphenylsilyl)phenyl]-phosphine oxide (TSPO1), 2,2′,2″-(1,3,5-benzinetriyl)tris(1-phenyl-1-*H*-benzimidazole) (TPBi), and lithium fluoride (LiF) were used for step by step depositions of the hole injecting layer (HIL), the hole transporting layers (HTL), hole blocking layer (HBL), electron transport layer (ETL), and electron injecting layer (EIL), respectively. The layers of ITO and Al served as the anode and cathode, respectively. Except for the light-emitting layers (EMLs), all the functional layers of devices A−D were simultaneously deposited. At least six pixels of each device were tested (see the "Organic light-emitting diodes" section in the Supporting information). Owing to the TSPO1 layer, the interface exciplex formation was excluded.

EL spectra of OLEDs A−D mostly resulted from the emission of Ir(piq)$_2$acac peaked at 630 nm.[32] EL spectra of devices A−D were characterized by the slightly different full width at half maxima (fwhm), apparently because of the different polarity of the hosts. Device B, with the highest fwhm of 96 nm, was characterized by the lowest EQE values and poorest host−guest energy transfer (Figure 5b, inset). In contrast to the EL spectra of reference OLED D, EL spectra of devices A−C were characterized by weak emission bands of the hosts with the intensity maxima at 440 nm (Figure 5b, inset). At 10 wt % of Ir(piq)$_2$acac, the complete host−guest energy transfer was not observed using hosts **4−6** apparently because of the presence of the relatively bulky groups −CF$_3$ or −C(CH$_3$)$_3$. Nevertheless, device C demonstrated a higher maximum EQE than reference device D due to the superior hosting properties of compound **6** in comparison to those of NPB (Figure 5c, Table 3). For the explanation of this

Table 3. Parameters of the OLEDs

device	A	B	C	D
host	**4**	**5**	**6**	NPB
V_{ON} (V) @ 10 cd/m^2	3.2	3.8	3.1	3.5
$V_{Driving}$ (V) @ 10 mA/cm^2	4.5	4.5	5.0	4.6
CE$_{max}$, cd/A	3.77	0.83	6.2	5.44
PE$_{max}$, lm/W	3.28	0.62	5.8	4.75
EQE$_{max}$, %	**4.77**	**1.31**	**8.0**	**6.83**
peak (nm) @ 1000 cd/m^2	628	632	629	630
fwhm (nm) @ 1000 cd/m^2	82	96	82	87
CIE (*x,y*) @ 1000 cd/m^2	(0.65, 0.32)	(0.64, 0.3)	(0.64, 0.31)	(0.68, 0.32)

observation, we have to refer to the IP$_{film}$ and EA$_{film}$ values of **6** (5.3 and 2.19 eV) and NPB (5.4 and 2.4 eV) (Figure 5a). The IP$_{film}$ and EA$_{film}$ values of both the compounds fit well to the corresponding characteristics of Ir(piq)$_2$acac, which are of 5.1 eV and 3.1 eV, respectively. The charge-injecting abilities of **6** and NPB did not affect much the EQE values of the devices.

Bipolar charge transport in the layer of NPB with a well-balanced hole and electron mobility of ca. $(5−6) \times 10^{-4}$ cm^2 V^{-1} s^{-1} at an electric field of 3.6×10^5 V·cm^{-1} was previously reported.[33] We obtained practically the same values of 6.2×10^{-4} cm^2 V^{-1} s^{-1} of hole mobility for the layer of compound **6** at the same electric field of 3.6×10^5 V·cm^{-1} (Figure 4d, Table 2). The precise analysis of charge-transporting properties of **6** and NPB indicates that the field-dependent parameter β of **6** $((6.9−7.6) \times 10^{-3}$ (cm V^{-1})$^{1/2})$ is much higher than that of ca. 3×10^{-3} (cm V^{-1})$^{1/2}$ observed for NPB.[34] These differences between β values of **6** and NPB mean that charge carrier transport of **6** is much more disperse than that of NPB. The charge transport dispersity of **6** can lead to the broader recombination zone in the EML of device C than in the NPB-based EML of device D. The different charge transport dispersity of **6** and NPB could be the main reasons for the differences in EQE values and efficiency roll-off of devices C and D. Apparently, the presence of −CF$_3$ groups in the molecules of hosts **4** and **5** results in lower EQEs of devices A and B in comparison to those of **6**- and NPB-based OLEDs (Figure 5c).

The current density of 10 mA/cm^2 was observed for devices A and B at lower driving voltages of 4.5 V than for OLEDs C and D (Figure 5d, Table 3). This observation is in agreement with the results of a charge mobility study performed for **4−6** and NPB. The highest hole and electron mobilities were observed for the layer of compound **4** (Figure 4d). However, the dark current densities at 0.5 V bias were found to be 6.4×10^{-8} mA·cm^{-2} for **6**, 2.4×10^{-4} mA·cm^{-2} for **4**, 2.3×10^{-4} mA·cm^{-2} for NPB, and 3×10^{-5} mA·cm^{-2} for **5**. Practically the same trend was observed for EQEs: 8% for **6**-based device C, 6.83% for **NPB**-based device D, 4.77% for **4**-based device A, and 1.31% for **5**-based device A (Figure 5c, Table 3). Comparison of EQEs of OLEDs C and D shows that compound **6**, containing −C(CH$_3$)$_3$ moieties, exhibited better hosting properties than NPB. The EQE of OLED C was found to be about 17% higher than that of device D. This efficiency enhancement can be partly related to the ultralow dark current density of the **6**-based OLED. This observation allows us to conclude that there was no leakage of charges without emissive recombination in device C. Device B showed the highest dark current density, leading to the lowest EQEs. This observation can be partly attributed to the leakage of charges without emissive recombination. The lowest turn-on voltage was observed for OLED C apparently because of the most balanced hole and electron transport of **6** within a wide range of electric fields (Figure 4d). Taking into account the ultralow dark current density, low turn-on voltage, and efficiencies of the fabricated devices, it can be concluded that compound **6** has the greatest potential to be widely used in OLEDs.

Organic Photodetectors. The performance of **4−6** in the OPD was investigated and compared with that of the conventional hole-transporting material (HTM) TAPC. The device structure ITO/**HTM**[95%]:C70[5%][150 nm]/Al[100 nm] was selected (Figure 6a). We labeled devices containing HTM **4**, **5**, **6**, or TAPC as I, II, III, and IV, respectively. The similar ultraviolet OPDs were previously investigated using TAPC and C60 for the deposition of an active layer.[14] Those OPDs showed ultrahigh EQEs of 1.08×10^6% under −14 V bias. However, the reverse bias dark current density was very high (ca. 2 mA·cm^{-2} at −14 V) for OPDs based on the mixture of TAPC and C60.[14] High dark current density at reverse bias
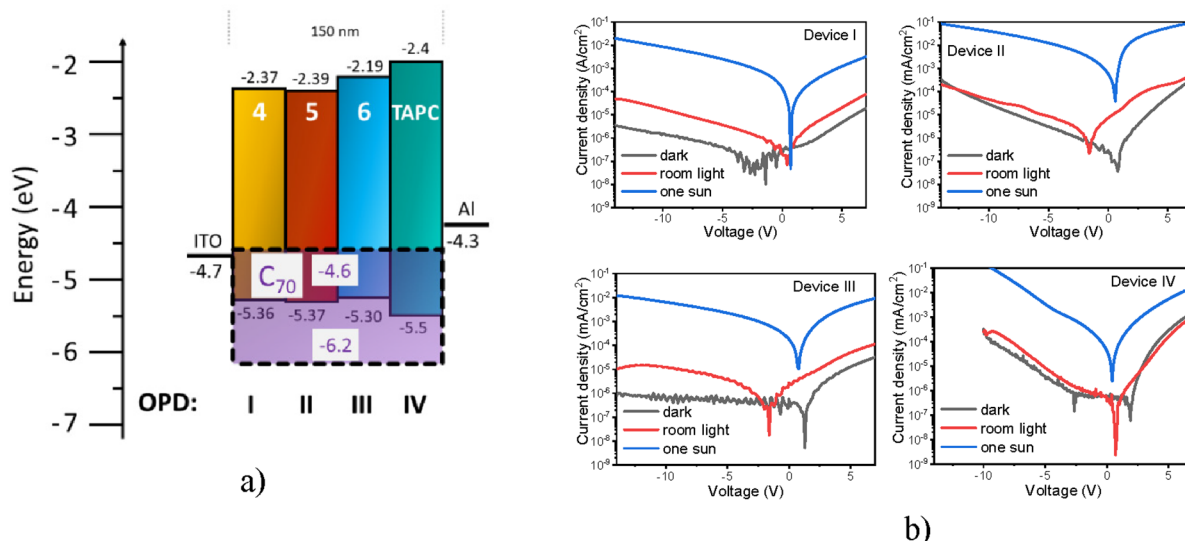
Figure 6. Equilibrium energy diagrams (a) and current density as a function of different voltages (b) in the dark, at 0.5 mW/cm^2 (indoor light), and at 100 mW/cm^2 (one sun at AM 1.5 G condition) conditions of devices I−IV.

limits the practical application of OPDs.[12,15] Similarly to the OPDs based on TAPC and C60,[14] the reference device IV based on the mixture of TAPC and C70 showed relatively high values of dark current density of 3×10^{-4} mA·cm^{-2} at the reverse bias of −10 V (Figure 6b). Low dark current densities of 1.4×10^{-6}, 2.5×10^{-5}, and 4.5×10^{-7} mA·cm^{-2} were obtained at −10 V for devices I−III containing HTM **4**−**6**, respectively (Figure 6b). The lowest dark current density was obtained when compound **6** was used as an HTM for the deposition of active layers of the OPDs. This result is in agreement with the lowest dark current density of OLED C based on compound **6** used as the host for the deposition of EML (Figure 5d). It should be noted that the dark current densities of the OPD containing compound **6** remain low in a wide range of reverse bias voltages (Figure 6b). Taking into account the limitation of the Keithley 2400 source meter used, we expected that the dark current densities of compound **6** are even lower than those shown in Figure 6b. The photocurrent densities recorded for devices I−IV under the AM 1.5 G condition at one sun of irradiance (100 mW/cm^2) at the reverse bias of −10 V were found to be 8.6×10^{-3}, 0.038, 6.5×10^{-3}, and 0.13 mA·cm^{-2}, respectively. The corresponding ratios of the photocurrent density recorded at 100 mW/cm^2 to the dark current density for devices I−IV at the same voltage were found to be 6×10^3, 1.5×10^3, 1.4×10^4, and 43.3, respectively. The corresponding ratios of the photocurrent density recorded in indoor light (0.5 mW/cm^2) to the dark current density were recorded to be 13.1, 1.9, 25.1, and 1.1, respectively. These ratios represent the relative photosensitivity of the studied OPDs. It should be noted that devices I−III showed better photosensitivity in comparison to that of the reference device IV. This allows us to claim that compounds **4**−**6** are more promising as HTM for the fabrication of active layers of OPDs than TAPC. Device III showed the highest photosensitivity, followed by devices I and II. This trend is the same as that of efficiencies of OLEDs C, A, and B (Figure 5c). This observation shows that the electronic properties of compound **6** are the most suitable for both the OLEDs and the OPDs.

Taking into account the advanced performance of compound **6** in OLEDs and OPDs, the following modification

of HTMs, including derivatives of 2,7-di-*tert*-butyl-9,9-dimethyl-9,10-dihydroacridine and phenanthroimidazole, should be performed using *tert*-butyl groups rather than trifluoro methyl moieties.

■ CONCLUSIONS

We have designed and synthesized three derivatives of 2,7-di-*tert*-butyl-9,9-dimethyl-9,10-dihydroacridine and phenanthroimidazole as bipolar organic semiconductors. The target compounds were obtained by Buchwald−Hartwig amination reactions with yields of up to 77%. The applicability of the compounds in electroluminescent devices and organic photodetectors is demonstrated. The compounds show high and balanced hole and electron mobilities, reaching 10^{-3} cm^2/V·s under strong electric fields. They also exhibit favorable energy levels for hole and electron injection/extraction, i.e., ionization potentials close to 5.3 eV, electron affinities close to 2.3 eV, and moderate triplet energies close to 2.7 eV. The compounds are capable of glass formation. Their glass transition temperatures are above 200 °C. The layers of the compounds are transparent in the visible region. Their absorption edges are at 400 nm. The preliminary tests of the developed bipolar organic semiconductors in organic photodetectors and organic light-emitting diodes revealed their ability to prevent high dark currents of devices until injection from electrodes occurred. One compound containing *tert*-butyl groups demonstrates the lowest dark current densities in both types of devices. This compound allows us to reach the best photosensitivity of organic photodetectors and the highest efficiency of organic light-emitting diodes. This work suggests the direction of development of organic bipolar semiconductors for efficient electroluminescent devices and organic photoconductors driven at an ultralow dark current density.

■ ASSOCIATED CONTENT

ⓢ Supporting Information

The Supporting Information is available free of charge at https://pubs.acs.org/doi/10.1021/acsaelm.4c00746.

Copies of NMR spectra, detailed descriptions of the synthesis and identification, general experimental in-

formation, DSC curves, and additional photophysical/ DFT/CELIV/TOF/OLED and OPD data (PDF)

■ AUTHOR INFORMATION

Corresponding Author

    Juozas V. Grazulevicius − *Department of Polymer Chemistry and Technology, Faculty of Chemical Technology, Kaunas University of Technology, LT-51423 Kaunas, Lithuania;* Email: juozas.grazulevicius@ktu.lt

Authors

    Rita Butkute − *Department of Polymer Chemistry and Technology, Faculty of Chemical Technology, Kaunas University of Technology, LT-51423 Kaunas, Lithuania*

    Ausrine Masiulyte − *Department of Polymer Chemistry and Technology, Faculty of Chemical Technology, Kaunas University of Technology, LT-51423 Kaunas, Lithuania*

    Ehsan Ullah Rashid − *Department of Polymer Chemistry and Technology, Faculty of Chemical Technology, Kaunas University of Technology, LT-51423 Kaunas, Lithuania*

    Svetlana Sargsyan − *Department of Organic Chemistry, Faculty of Chemistry, Yerevan State University, Yerevan 0025, Armenia*

    Neelalohith Satish Moudgalya − *Department of Polymer Chemistry and Technology, Faculty of Chemical Technology, Kaunas University of Technology, LT-51423 Kaunas, Lithuania*

    Karolis Leitonas − *Department of Polymer Chemistry and Technology, Faculty of Chemical Technology, Kaunas University of Technology, LT-51423 Kaunas, Lithuania*

    Dmytro Volyniuk − *Department of Polymer Chemistry and Technology, Faculty of Chemical Technology, Kaunas University of Technology, LT-51423 Kaunas, Lithuania;* orcid.org/0000-0003-3526-2679

Complete contact information is available at: https://pubs.acs.org/10.1021/acsaelm.4c00746

Author Contributions

R.B., D.V., and J.V.G. designed the research. R.B., A.M., and N.S.M. performed the synthesis, K.L. and D.V. were responsible for the photophysical studies, R.B. and N.S.M. were responsible for thermal analyses and electrochemical investigations, and E.U.R. performed DFT calculations. D.V., K.L., and D.V. characterized charge transporting properties, K.L. and D.V. investigated devices, and R.B., D.V., and J.V.G. wrote the manuscript with support and contributions from all authors.

Notes

The authors declare no competing financial interest.

■ REFERENCES

(1) Yeon, H.; Lee, H.; Kim, Y.; Lee, D.; Lee, Y.; Lee, J.-S.; Shin, J.; Choi, C.; Kang, J.-H.; Suh, J. M.; Kim, H.; Kum, H. S.; Lee, J.; Kim, D.; Ko, K.; Ma, B. S.; Lin, P.; Han, S.; Kim, S.; Bae, S.-H.; Kim, T.-S.; Park, M.-C.; Joo, Y.-C.; Kim, E.; Han, J.; Kim, J. Long-term reliable physical health monitoring by sweat pore−inspired perforated electronic skins. *Sci. Adv.* **2021**, 7, No. eabg8459.

(2) Shi, Ch.; Zou, Z.; Lei, Z.; Zhu, P.; Zhang, W.; Xiao, J. Heterogeneous integration of rigid, soft, and liquid materials for self-healable, recyclable, and reconfigurable wearable electronics. *Sci. Adv.* **2020**, 6, No. eabd0202.

(3) Li, N.; Wang, Q.; Shen, C.; Wei, Z.; Yu, H.; Zhao, J.; Lu, X.; Wang, G.; He, C.; Xie, L.; Zhu, J.; Du, L.; Yang, R.; Shi, D.; Zhang, G. Large-scale flexible and transparent electronics based on monolayer molybdenum disulfide field-effect transistors. *Nat. Electron.* **2020**, 3, 711−717.

(4) Chow, P. C. Y.; Someya, T. Organic Photodetectors for Next-Generation Wearable Electronics. *Adv. Mater.* **2020**, 32, 1902045.

(5) Lee, H.; Jiang, Z.; Yokota, T.; Fukuda, K.; Park, S.; Someya, T. Stretchable organic optoelectronic devices: Design of materials, structures, and applications. *Mater. Sci. Eng. R* **2021**, 146, 100631.

(6) dos Santos, P. L.; Stachelek, P.; Takeda, Y.; Pander, P. Recent advances in highly-efficient near infrared OLED emitters. *Mater. Chem. Front.* **2024**, 8, 1731.

(7) Miao, W.-C.; Hsiao, F.-H.; Sheng, Y.; Lee, T.-Y.; Hong, Y.-H.; Tsai, C.-W.; Chen, H.-L.; Liu, Z.; Lin, C.-L.; Chung, R.-J.; Ye, Z.-T.; Horng, R.-H.; Chen, S.-C.; Kuo, H.-C.; He, J.-H. Microdisplays: Mini-LED, Micro-OLED, and Micro-LED. *Adv. Optical Mater.* **2024**, 12, 2300112.

(8) Lee, J.-H.; Chen, C.-H.; Lee, P.-H.; Lin, H.-Y.; Leung, M.; Chiu, T.-L.; Lin, C.-F. Blue organic light-emitting diodes: current status, challenges, and future outlook. *J. Mater. Chem. C* **2019**, 7, 5874−5888.

(9) Woo, J. Y.; Park, M.-H.; Jeong, S.-H.; Kim, Y.-H.; Kim, B.; Lee, T.-W.; Han, T.-H. Advances in Solution-Processed OLEDs and their Prospects for Use in Displays. *Adv. Mater.* **2023**, 35, 2207454.

(10) Nayak, D.; Choudhary, R. B. Asurveyofthestructure, fabrication, and characterization of advanced organic light emitting diodes. *Microelectron. Reliab.* **2023**, 144, 114959.

(11) Kumar, K. Charge transporting and thermally activated delayed fluorescence materials for OLED applications. *Phys. Chem. Chem. Phys.* **2024**, 26, 3711−3754.

(12) Wang, C.; Zhang, X.; Hu, W. Organic photodiodes and phototransistors toward infrared detection: materials, devices, and applications. *Chem. Soc. Rev.* **2020**, 49, 653−670.

(13) Chow, P. C. Y.; Someya, T. Organic Photodetectors for Next-Generation Wearable Electronics. *Adv. Mater.* **2020**, 32, 1902045.

(14) Guo, D.; Yang, L.; Zhao, J.; Li, J.; He, G.; Yang, D.; Wang, L.; Vadim, A.; Ma, D. Visible-blind ultraviolet narrowband photo-multiplication-type organic photodetector with an ultrahigh external quantum efficiency of over 1000000%. *Mater. Horiz.* **2021**, 8, 2293−2302.

(15) Ma, X.; Bin, H.; van Gorkom, B. T.; van der Pol, T. P. A.; Dyson, M. J.; Weijtens, C. H. L.; Fattori, M.; Meskers, S. C. J.; van Breemen, A. J. J. M.; Tordera, D.; Janssen, R. A. J.; Gelinck, G. H. Identification of the Origin of Ultralow Dark Currents in Organic Photodiodes. *Adv. Mater.* **2023**, 35, 2209598.

(16) Jang, W.; Kim, B. G.; Seo, S.; Shawky, A.; Kim, M. S.; Kim, K.; Mikladal, B.; Kauppinen, E. I.; Maruyama, S.; Jeon, I.; Wang, D. H. Strong dark current suppression in flexible organic photodetectors by carbon nanotube transparent electrodes. *Nano Today* **2021**, 37, 101081.

(17) Aydemir, M.; Haykır, G.; Battal, A.; Jankus, V.; Sugunan, S. K.; Dias, F. B.; Al-Attar, H.; Türksoy, F.; Tavaslı, M.; Monkman, A. P. High efficiency OLEDs based on anthracene derivatives: The impact of electron donating and withdrawing group on the performance of OLED. *Org. Electron.* **2016**, 30, 149−157.

(18) Peddis, D.; Cannas, C.; Musinu, A.; Ardu, A.; Orrù, F.; Fiorani, D.; Laureti, S.; Rinaldi, D.; Muscas, G.; Concas, G.; Piccaluga, G. Beyond the Effect of Particle Size: Influence of CoFe2O4Nanoparti-cleArrangements on Magnetic Properties. *Chem. Mater.* **2013**, 25, 2005−2013.

(19) Obolda, A.; Peng, Q.; He, C.; Zhang, T.; Ren, J.; Ma, H.; Shuai, Z.; Li, F. Triplet−Polaron-Interaction-Induced Upconversion from Triplet to Singlet: a Possible Way to Obtain Highly Effi cient OLEDs. *Adv. Mater.* **2016**, 28, 4740−4746.

(20) Liu, H.; Kang, L.; Li, J.; Liu, F.; He, X.; Ren, S.; Tang, X.; Lv, C.; Lu, P. Highly efficient deep-blue organic light-emitting diodes

based on pyreno[4,5-d]imidazole-anthracene structural isomers. *J. Mater. Chem. C* **2019**, *7*, 10273−10280.

(21) Tang, X. Y.; Bai, Q.; Shan, T.; Li, J.; Gao, Y.; Liu, F.; Liu, H.; Peng, Q.; Yang, B.; Li, F.; Lu, P. Efficient Nondoped Blue Fluorescent Organic Light-Emitting Diodes (OLEDs) with a High External Quantum Efficiency of 9.4% @ 1000 cd m−2 Based on Phenanthroimidazole−Anthracene Derivative. *Adv. Funct. Mater.* **2018**, *28*, 1705813.

(22) Richaud, A.; Barba-Behrens, N.; Méndez, F. Chemical Reactivity of the Imidazole:A Semblance of Pyridine and Pyrrole? *Org. Lett.* **2011**, *13* (5), 972−975.

(23) Tagare, J.; Vaidyanathan, S. Recent development of phenanthroimidazolebased fluorophores for blue organic light-emitting diodes (OLEDs): an overview. *J. Mater. Chem. C* **2018**, *6*, 10138−10173.

(24) Chen, W.-C.; Yuan, Y.; Xiong, Y.; Rogach, A. L.; Tong, Q.-X.; Lee, C.-S. Aromatically C6- and C9-Substituted Phenanthro[9,10-d]imidazole Blue Fluorophores: Structure−Property Relationship and Electroluminescent Application. *ACS Appl. Mater. Interfaces* **2017**, *9*, 26268−26278.

(25) Conboy, G.; Spencer, H. J.; Angioni, E.; Kanibolotsky, A. L.; Findlay, N. J.; Coles, S. J.; Wilson, C.; Pitak, M. B.; Risko, C.; Coropceanu, V.; Brédas, J.-L.; Skabara, P. To bend or not to bend— are heteroatom interactions within conjugated molecules effective in dictating conformation and planarity? *Mater. Horiz.* **2016**, *3*, 333− 339.

(26) Sakamoto, Y.; Suzuki, T.; Kobayashi, M.; Gao, Y.; Fukai, Y.; Inoue, Y.; Sato, F.; Tokito, S. Perfluoro-pentacene: High-Performance p−n Junctions and Complementary Circuits with Pentacene. *J. Am. Chem. Soc.* **2004**, *126*, 8138−8140.

(27) Chen, Z.; Zhang, W.; Huang, J.; Gao, D.; Wei, C.; Lin, Z.; Wang, L.; Yu, G. Fluorinated Dithienyl-ethene−Naphthalenediimide Copolymers forHigh-Mobility n-Channel Field-Effect Transistors. *Macromolecules* **2017**, *50*, 6098−6107.

(28) Carroll, T. X.; Thomas, T. D.; Bergersen, H.; Børve, K. J.; Sæthre, L. J. Fluorine as a π Donor. Carbon 1s Photoelectron Spectroscopy and Proton Affinities of Fluorobenzenes. *J. Org. Chem.* **2006**, *71*, 1961−1968.

(29) Sharber, S. A.; Baral, R. N.; Frausto, F.; Haas, T. E.; Müller, P.; Thomas, S. W., III Substituent Effects That Control Conjugated Oligomer Conformation through Non-covalent Interactions. *J. Am. Chem. Soc.* **2017**, *139*, 5164−5174.

(30) Stephen, M.; Genevičius, K.; Juška, G.; Arlauskas, K.; Hiorns, R. C. Charge transport and its characterization usingphoto-CELIV in bulk heterojunction solar cells. *Polym. Int.* **2017**, *66*, 13−25.

(31) Park, Y.; Lee, G. S.; Lee, W.; Yoo, S.; Kim, Y.-H.; Choi, K.-C. Heteroleptic Ir(III)-based near-infrared organic light-emitting diodes with high radiance capacity. *Sci. Rep.* **2023**, *13*, 1369.

(32) Gnanasekaran, P.; Chen, Y.-T.; Tseng, Y.-T.; Su, K.-Y.; Lin, Y.-T.; Yiu, T. C.; Chang, C.-H.; Chang, Y. J. Perceiving the influence of phenyl-carbazole isomers on sulfone/thioxanthone-based D−A−D hosts: realizing efficient red-phosphorescent OLEDs. *J. Mater. Chem. C* **2024**, *12*, 2203−2215.

(33) Tse, S. C.; Kwok, K. C.; So, S. K. Electron transport in naphthylamine-based organic compounds. *Appl. Phys. Lett.* **2006**, *89*, 262102.

(34) Tsung, K. K.; So, S. K. Carrier trapping and scattering in amorphous organic hole transporter. *Appl. Phys. Lett.* **2008**, *92*, 103315.